22. Fountain, G. O., Khakhar, D. V. & Ottino, J. M. Visualization of three-dimensional chaos. *Science* **281,** 683–686 (1998).
23. Shinbrot, T., Alvarez, M. M., Zalc, J. M. & Muzzio, F. J. Attraction of minute particles to invariant regions of volume preserving flows by transients. *Phys. Rev. Lett.* **86,** 1207–1210 (2001).
24. Vainshtein, D. L., Vasiliev, A. A. & Neishtadt, A. J. Changes in the adiabatic invariant and streamline chaos in confined incompressible Strokes flow. *Chaos* **6,** 67–77 (1996).
25. Clever, R. M. & Busse, F. H. Transition to time-dependent convection. *J. Fluid Mech.* **65,** 625–645 (1974).
26. Solomon, T. H. & Gollub, J. P. Chaotic particle transport in time-dependent Rayleigh-Bénard convection. *Phys. Rev. A.* **38,** 6280–6286 (1988).
27. Chandresekhar, S. *Hydrodynamic and Hydromagnetic Stability* 39 (Clarendon, Oxford, 1961).
28. Solomon, T. H., Tomas, S. & Warner, J. L. The role of lobes in chaotic mixing of miscible and immiscible impurities. *Phys. Rev. Lett.* **77,** 2682–2685 (1996).
29. Solomon, T. H., Tomas, S. & Warner, J. L. Chaotic mixing of immiscible and immiscible impurities in a two-dimensional flow. *Phys. Fluids* **10,** 342–350 (1998).
30. Cussler, E. L. *Diffusion: Mass Transfer in Fluid Systems* (Cambridge Univ. Press, Cambridge, 1984).

Supplementary Information accompanies the paper on **www.nature.com/nature**.

Acknowledgements This work was supported by the US National Science Foundation, AFOSR, and by a Sloan Fellowship grant.

Competing interests statement The authors declare that they have no competing financial interests.

Correspondence and requests for materials should be addressed to T.S. (tsolomon@bucknell.edu) or I.M. (mezic@engineering.ucsb.edu).

Microwave oscillations of a nanomagnet driven by a spin-polarized current

S. I. Kiselev[1]*, J. C. Sankey[1]*, I. N. Krivorotov[1], N. C. Emley[1], R. J. Schoelkopf[2], R. A. Buhrman[1] & D. C. Ralph[1]

[1]*Cornell University, Ithaca, New York 14853, USA*
[2]*Department of Applied Physics and Physics, Yale University, New Haven, Connecticut 06511, USA*

* These authors contributed equally to this work

The recent discovery that a spin-polarized electrical current can apply a large torque to a ferromagnet, through direct transfer of spin angular momentum, offers the possibility of manipulating magnetic-device elements without applying cumbersome magnetic fields[1–16]. However, a central question remains unresolved: what type of magnetic motions can be generated by this torque? Theory predicts that spin transfer may be able to drive a nanomagnet into types of oscillatory magnetic modes not attainable with magnetic fields alone[1–3], but existing measurement techniques have provided only indirect evidence for dynamical states[4,6–8,12,14–16]. The nature of the possible motions has not been determined. Here we demonstrate a technique that allows direct electrical measurements of microwave-frequency dynamics in individual nanomagnets, propelled by a d.c. spin-polarized current. We show that spin transfer can produce several different types of magnetic excitation. Although there is no mechanical motion, a simple magnetic-multilayer structure acts like a nanoscale motor; it converts energy from a d.c. electrical current into high-frequency magnetic rotations that might be applied in new devices including microwave sources and resonators.

We examine samples made by sputtering a multilayer of composition 80 nm Cu/40 nm Co/10 nm Cu/3 nm Co/2 nm Cu/30 nm Pt onto an oxidized silicon wafer and then milling through part of the multilayer (Fig. 1a) to form a pillar with an elliptical cross-section of lithographic dimensions 130 nm × 70 nm (ref. 17). Top contact is made with a Cu electrode. Transmission or reflection of electrons from the thicker 'fixed' Co layer produces a spin-polarized current that can apply a torque to the thinner 'free' Co layer. Subsequent oscillations of the free-layer magnetization relative to the fixed layer change the device resistance[18] so, under conditions of d.c. current bias, magnetic dynamics produce a time-varying voltage (with typical frequencies in the microwave range). If the oscillations were exactly symmetric relative to the direction of the fixed-layer moment, voltage signals would occur only at multiples of twice the fundamental oscillation frequency, f. To produce signal strength at f, we apply static magnetic fields (H) in the sample plane a few degrees away from the magnetically easy axis of the free layer. All data are taken at room temperature, and by convention positive current I denotes electron flow from the free to the fixed layer.

In characterization measurements done at frequencies <1 kHz, the samples exhibit the same spin-transfer-driven changes in resistance reported in previous experiments[7,9] (Fig. 1b). For H smaller than the coercive field of the free layer ($H_c \approx 600$ Oe), an applied current produces hysteretic switching of the magnetic layers between the low-resistance parallel (P) and high-resistance antiparallel (AP) states. Sweeping H can also drive switching between the P and AP states (Fig. 1b, inset). For H larger than 600 Oe, the current produces peaks in the differential resistance dV/dI that have been assumed previously to be associated with dynamical magnetic excitations[4,6–8]. The resistance values displayed in Fig. 1b include a lead resistance of $\sim 6\,\Omega$ from high-frequency (50 GHz) probes and a top-contact resistance of $\sim 9\,\Omega$.

We measure the spectra of microwave power that result from magnetic motions by using a heterodyne mixer circuit[19] (Fig. 1a). This circuit differs from the only previous experiment to probe spin-transfer-driven magnetic oscillations[8] in that the sample is not exposed to a large high-frequency magnetic field that would alter its dynamics. The filter on the output of our mixer passes 25–100 MHz, giving a frequency resolution of ~ 200 MHz. We calibrate the circuit by measuring temperature-dependent Johnson noise from test resistors. When we state values of emitted power, they will correspond to the power available to a load matched to the sample resistance, R. To convert to the power delivered to a 50-Ω line, one should multiply our values by the power transmission coefficient $1 - \Gamma^2 = 1 - [(R - 50\ \Omega)/(R + 50\ \Omega)]^2$.

We first consider the microwave spectrum from sample 1 for $H = 2$ kOe. For both negative I and small positive I we measure only frequency-independent Johnson noise. We will subtract this background from all the spectra we display. At $I = 2.0$ mA, we begin to resolve a microwave signal at 16.0 GHz (Fig. 1c, d). A second-harmonic peak is also present (Fig. 1c, inset). As I is increased, these initial signals grow until $I \approx 2.4$ mA, beyond which the dynamics change to a different regime (Fig. 1d). In Fig. 1e, we compare the H-dependence of the measured frequency for the initial signals to the formula for small-angle elliptical precession of a thin-film ferromagnet[20]:

$$f = \frac{\gamma}{2\pi}\sqrt{(H + H_{an} + H_d)(H + H_{an} + H_d + 4\pi M_{eff})} \qquad (1)$$

Here γ is the gyromagnetic ratio, H_{an} accounts for a uniaxial easy-axis anisotropy, H_d models the coupling from the fixed layer, and $4\pi M_{eff} = 4\pi M_s - 2K_u/M_s$, with M_s the saturation magnetization and K_u a uniaxial perpendicular anisotropy[21]. The fit is excellent and gives the values $4\pi M_{eff} = 6.8 \pm 0.1$ kOe and $H_{an} + H_d = 1.18 \pm 0.04$ kOe. The value for $4\pi M_{eff}$ is less than $4\pi M_s$ for bulk Co (16 kOe) as expected due to significant perpendicular anisotropy in Co/Cu(111) films (see Fig. 3 in ref. 22). Similar fits for other samples yield $4\pi M_{eff}$ in the range 6.7–12 kOe. Superconducting quantum interference device (SQUID) measurements on test samples containing many 3-nm Co layers give $4\pi M_{eff} = 10 \pm 1$ kOe.

On the basis of the agreement with equation (1) we identify the initial signals as arising from small-angle elliptical precession of the free layer, thereby confirming pioneering predictions that spin-transfer can coherently excite this uniform spin-wave mode[2]. We can make a rough estimate for the amplitude of the precession angle, θ_{max}, and the misalignment θ_{mis} between the precession axis and the fixed-layer moment (induced by the applied field), based on the integrated microwave power measured about f and $2f$ (P_f and P_{2f}). Assuming for simplicity that $\theta(t) = \theta_{mis} + \theta_{max}\sin(\omega t)$, that the angular variation in resistance $\Delta R(\theta) = \Delta R_{max}(1 - \cos(\theta))/2$, and that $|\theta_{mis} \pm \theta_{max}| \ll 1$, we calculate:

$$\theta_{max}^4 \approx \frac{512 P_{2f} R}{\Delta R_{max}^2 I^2} \quad (2)$$

$$\theta_{mis}^2 \approx \frac{32 P_f R}{\Delta R_{max}^2 I^2 \theta_{max}^2} \quad (3)$$

where $R = 12.8\,\Omega$ and $\Delta R_{max} = 0.11\,\Omega$ is the resistance change between P and AP states. For the spectrum from sample 1 in the inset to Fig. 1c, we estimate that $\theta_{mis} \approx 9°$, and the precessional signal first becomes measurable above background when $\theta_{max} \approx 10°$.

With increasing currents, the nanomagnet exhibits additional dynamical regimes. As I is increased beyond 2.4 mA to 3.6 mA for sample 1, the microwave power grows by two orders of magnitude, peak frequencies shift abruptly, and the spectrum acquires a significant low-frequency background (Fig. 1c). In many samples (including sample 2 below) the background becomes so large that some spectral peaks are difficult to distinguish. Within this large-amplitude regime, peaks shift down in frequency with increasing current (Fig. 1f). The large-amplitude signals persist for I up to 6.0 mA, where the microwave power plummets sharply at the same current for which there is a shoulder in dV/dI. The state that appears thereafter has a d.c. resistance 0.04 Ω lower than the AP state and

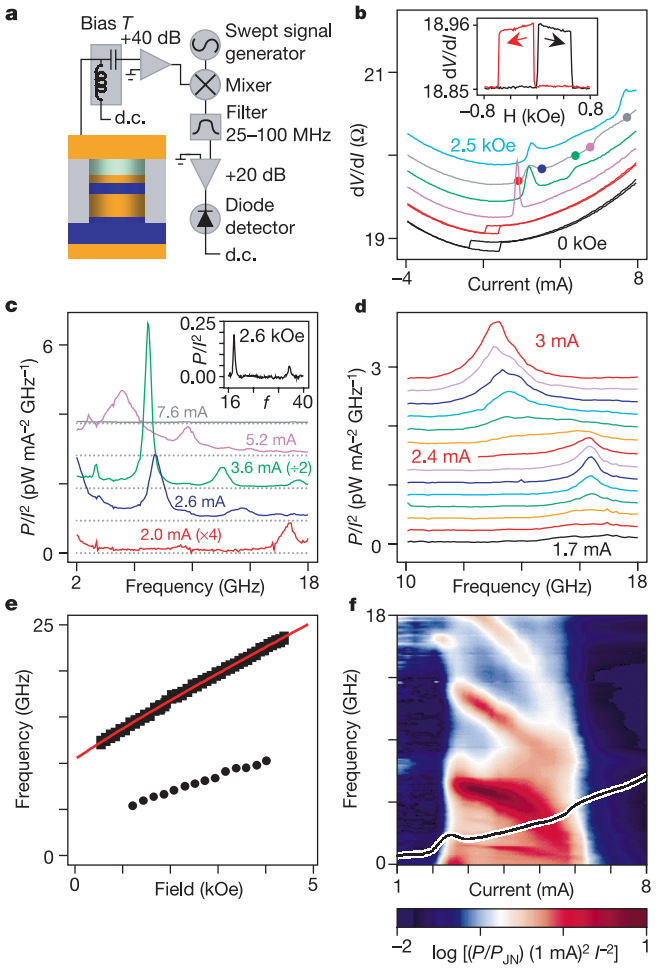

Figure 1 Resistance and microwave data for sample 1. **a**, Schematic of the sample with copper layers (orange), cobalt (blue), platinum (green) and SiO_2 insulator (grey), together with the heterodyne mixer circuit. Different preamplifiers and mixers allow measurements over 0.5–18 GHz or 18–40 GHz. **b**, Differential resistance versus current for magnetic fields of 0 (bottom), 0.5, 1.0, 1.5, 2.0 and 2.5 kOe (top), with current sweeps in both directions. At $H = 0$, the switching currents are $I_c^+ = 0.88$ mA and $I_c^- = -0.71$ mA, and $\Delta R_{max} = 0.11\,\Omega$ between the P and AP states. Coloured dots on the 2 kOe curve correspond to spectra shown in **c**. Inset to **b**, Magnetoresistance near $I = 0$. Red and black indicate different directions of magnetic-field sweep. **c**, Microwave spectra (with Johnson noise subtracted) for $H = 2.0$ kOe, for $I = 2$ mA (bottom), 2.6, 3.6, 5.2 and 7.6 mA (top). We plot power density divided by I^2 to facilitate comparisons of the underlying changes in resistance at different current values. Inset to **c**, Spectrum at $H = 2.6$ kOe and $I = 2.2$ mA, for which both f and $2f$ peaks are visible on the same scan. **d**, Microwave spectra at $H = 2.0$ kOe, for current values from 1.7 to 3.0 mA in 0.1-mA steps, showing the growth of the small-amplitude precessional peak and then a transition in which the second harmonic signal of the large-amplitude regime appears. **e**, Magnetic-field dependence of the small-amplitude signal frequency (top) and the frequency of the fundamental in the large-amplitude regime at $I = 3.6$ mA (bottom). The line is a fit to equation (1). **f**, Microwave power density (in colour scale) versus frequency and current for $H = 2.0$ kOe. The black line shows dV/dI versus I from **b**. P_{JN} is the Johnson-noise power level. The curves in **b**, **c** and **d** are offset vertically.

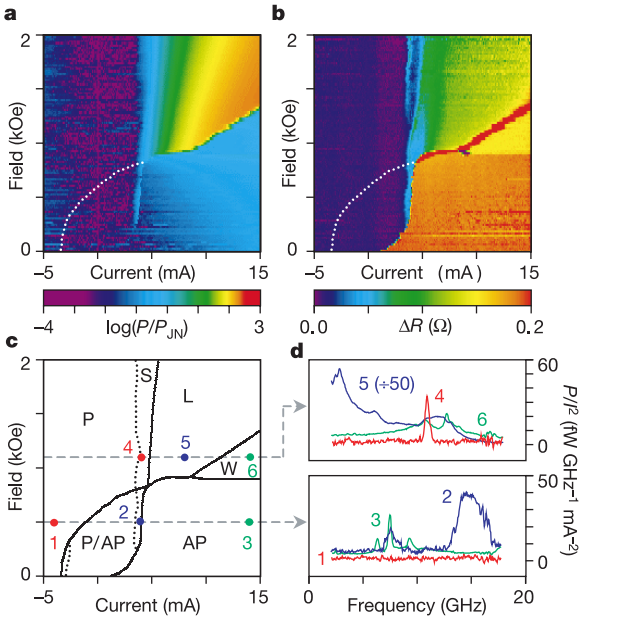

Figure 2 Resistance and microwave data for sample 2. Sample 2 has, at $H = 0$, $I_c^+ = 1.06$ mA, $I_c^- = -3.22$ mA, parallel-state resistance (including top-contact and lead resistances) 17.5 Ω, $\Delta R_{max} = 0.20\,\Omega$ between the P and AP states, and $4\pi M_{eff} = 12$ kOe. **a**, Microwave power above Johnson noise in the frequency range 0.1–18 GHz, plotted in colour scale versus I and H. I is swept from negative to positive values. These data were collected without the mixer circuit by measuring the power with a detector diode after amplification. The dotted white line shows the position of the AP to P transition when I is swept positive to negative. **b**, Differential resistance plotted in colour scale for the same region of I and H. A smooth current-dependent, H-independent background (similar to that of Fig. 1b) is subtracted to better display the different regimes of resistance. Resistance changes are measured relative to the parallel state. **c**, Room-temperature experimental dynamical stability diagram extracted from **a** and **b**. P indicates parallel orientation, AP antiparallel orientation, P/AP parallel/antiparallel bistability, S the small-amplitude precessional regime, L the large-amplitude dynamical regime, and W a state with resistance between P and AP and only small microwave signals. The coloured dots in **c** correspond to the microwave spectra at $H = 500$ and 1,100 Oe shown in **d**.

0.07 Ω above the P state. At even higher current levels (not shown), we sometimes see additional large microwave signals that are not reproducible from sample to sample. These might be associated with dynamics in the fixed layer.

The regions of I and H associated with each type of dynamical mode can be determined by analysing the microwave power and dV/dI (Fig. 2a, b for sample 2). In all eight samples that we have examined in detail, large microwave signals occur for a similarly shaped range of I and H. Samples 1 and 2 exhibit clear structure in dV/dI at the boundaries of the large-amplitude regime, but other samples sometimes lack prominent dV/dI features over part of this border. In Fig. 2c we construct a dynamical stability diagram showing the different modes that can be driven by a d.c. spin-transfer current and a constant in-plane magnetic field. Explaining the existence of all these modes and the positions of their boundaries will provide a rigorous testing ground for theories of spin-transfer-driven magnetic dynamics.

As indicated in Fig, 2c, d, microwave signals can sometimes be observed not only at large H where dynamical modes have been postulated previously[4,6–8,12,14–16], but also in the small-H regime of current-driven hysteretic switching. While sweeping to increasing currents at $H = 500$ Oe; for example, microwave peaks corresponding to small-angle precession exist for I within ~0.7 mA below the current for P to AP switching. Similar features are also observed before switching from AP to P at negative bias. We suggest that these microwave signals are due to fluctuations of the free-layer moment away from its easy axis to angles large enough to produce measurable precession, but too small to achieve full reversal over the activation barrier for switching[23]. Related signals have been observed recently in magnetic tunnel junctions[24].

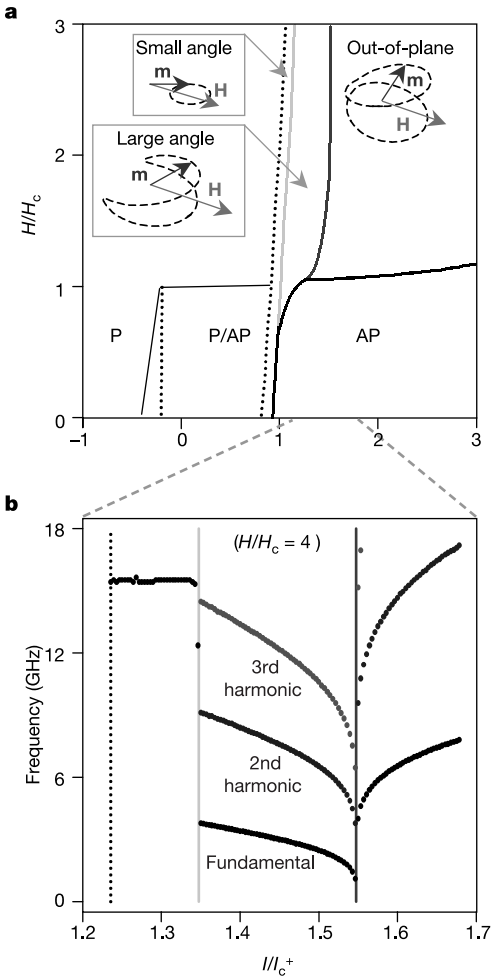

Figure 3 Results of numerical solution of the Landau–Lifshitz–Gilbert equation for a single-domain nanomagnet at zero temperature. The parameters are[1]: $4\pi M_{\mathrm{eff}} =$ 10 kOe, $H_{\mathrm{an}} = 500$ Oe, Gilbert damping parameter $\alpha = 0.014$, and effective polarization $P = 0.3$, which produce $H_{\mathrm{c}} = 500$ Oe and $I_{\mathrm{c}}^{+} = 2.8$ mA. **a**, Theoretical dynamical stability diagram. The pictures show representative orbits for the free-layer moment vector (**m**). **b**, Dependence of frequency on current in the simulation for $H = 2$ kOe, including both the fundamental frequency and harmonics in the measurement range.

To understand what type of motion may be associated with the different dynamical modes, we have computed solutions of the Landau–Lifshitz–Gilbert equation of motion for a single-domain magnet[25–28]. We employ the form of the spin-transfer torque derived in ref. 1. The calculated zero-temperature dynamical phase diagram is presented in Fig. 3a. We have not attempted to adjust parameters to fit our data, but nevertheless the existence and relative positions of the P, AP and small-angle-precession regimes agree well. The model suggests that the large-amplitude microwave signals correspond to large-angle, approximately in-plane precession of the free-layer moment. The simulation reproduces the abrupt jump to much lower frequency at the onset of this mode, decreasing frequency with further increases in current (Fig. 3b), and large powers in the harmonics. The maximum simulated microwave powers for this mode in the 0–18 GHz bandwidth are 18 pW mA^{-2} for sample 1 and 75 pW mA^{-2} for sample 2 (differing primarily because of different ΔR_{max} values), whereas the measured maxima are 10 and 90 pW mA^{-2}, respectively. Low-frequency backgrounds in the large-amplitude spectra (for example, Fig. 2d, spectrum 5) might be caused by fluctuations from the large-angle precessional orbit to other modes nearby in energy[28]. The single-domain simulation does not explain state W in Fig. 2c, but instead for that region it predicts approximately circular out-of-plane precessional modes. These would produce large microwave signals (~25–100 pW mA^{-2}), orders of magnitude larger than the residual signals observed in state W. We suspect that our single-domain approximation may become invalid in regime W owing to dynamical instabilities[29,30], so that different regions of the sample may move incoherently, giving total time-dependent resistance changes much smaller than for single-domain motion.

The microwave power generated by the precessing nanomagnet in our devices can be quite significant. For sample 1, the largest peak in the power spectrum has a maximum more than 40 times larger than room-temperature Johnson noise. Nanomagnets driven by spin-polarized currents might therefore serve as nanoscale microwave sources or oscillators, tunable by I and H over a wide frequency range. □

Received 28 May; accepted 28 July 2003; doi:10.1038/nature01967.

1. Slonczewski, J. C. Current-driven excitation of magnetic multilayers. *J. Magn. Magn. Mater.* **159,** L1–L7 (1996).
2. Berger, L. Emission of spin waves by a magnetic multilayer traversed by a current. *Phys. Rev. B* **54,** 9353–9358 (1996).
3. Bazaliy, Y. B., Jones, B. A. & Zhang, S. C. Modification of the Landau-Lifshitz equation in the presense of a spin-polarized current and colossal- and giant-magnetoresistive materials. *Phys. Rev. B* **57,** R3213–R3216 (1998).
4. Tsoi, M. *et al.* Excitation of a magnetic multilayer by an electric current. *Phys. Rev. Lett.* **80,** 4281–4284 (1998); erratum *Phys. Rev. Lett.* **81,** 493 (1998).
5. Sun, J. Z. Current-driven magnetic switching in manganite trilayer junctions. *J. Magn. Magn. Mater.* **202,** 157–162 (1999).
6. Myers, E. B., Ralph, D. C., Katine, J. A., Louie, R. N. & Buhrman, R. A. Current-induced switching of domains in magnetic multilayer devices. *Science* **285,** 867–870 (1999).
7. Katine, J. A., Albert, F. J., Buhrman, R. A., Myers, E. B. & Ralph, D. C. Current-driven magnetization reversal and spin-wave excitations in Co/Cu/Co pillars. *Phys. Rev. Lett.* **84,** 4212–4215 (2000).
8. Tsoi, M. *et al.* Generation and detection of phase-coherent current-driven magnons in magnetic multilayers. *Nature* **406,** 46–48 (2000).
9. Grollier, J. *et al.* Spin-polarized current induced switching in Co/Cu/Co pillars. *Appl. Phys. Lett.* **78,** 3663–3665 (2001).
10. Stiles, M. D. & Zangwill, A. Anatomy of spin-transfer torque. *Phys. Rev. B* **65,** 014407 (2002).
11. Wegrowe, J.-E. *et al.* Exchange torque and spin transfer between spin polarized current and ferromagnetic layers. *Appl. Phys. Lett.* **80,** 3775–3777 (2002).
12. Sun, J. Z., Monsma, D. J., Abraham, D. W., Rooks, M. J. & Koch, R. H. Batch-fabricated spin-injection magnetic switches. *Appl. Phys. Lett.* **81,** 2202–2204 (2002).

13. Bauer, G. E. W., Tserkovnyak, Y., Huertas-Hernando, D. & Brataas, A. Universal angular magnetoresistance and spin torque in ferromagnetic/normal metal hybrids. *Phys. Rev. B* **67,** 094421 (2003).
14. Rippard, W. H., Pufall, M. R. & Silva, T. J. Quantitative studies of spin-momentum-transfer-induced excitations in Co/Cu multilayer films using point-contact spectroscopy. *Appl. Phys. Lett.* **82,** 1260–1262 (2003).
15. Özyilmaz, B. *et al.* Current-induced magnetization reversal in high magnetic fields in Co/Cu/Co nanopillars. *Phys. Rev. Lett.* **91,** 067203 (2003).
16. Urazhdin, S., Birge, N. O., Pratt, W. P. Jr & Bass, J. Current-driven magnetic excitations in permalloy-based multilayer nanopillars. Preprint at ⟨http://arXiv:cond-mat/0303149⟩ (2003).
17. Albert, F. J. *The Fabrication and Measurement of Current Perpendicular to the Plane Magnetic Nanostructures for the Study of the Spin Transfer Effect*. PhD dissertation, Cornell Univ. (2003).
18. Baibich, M. N. *et al.* Giant magnetoresistance of (001)Fe/(001)Cr magnetic superlattices. *Phys. Rev. Lett.* **61,** 2472–2475 (1988).
19. Pozar, D. M. *Microwave Engineering* 2nd edn, 566 (John Wiley & Sons, New York, 1998).
20. Kittel, C. *Introduction to Solid State Physics* 7th edn, 505 (John Wiley & Sons, New York, 1996).
21. Johnson, M. T., Bloemen, P. J. H., den Broeder, F. J. A. & de Vries, J. J. Magnetic anisotropy in metallic multilayers. *Rep. Prog. Phys.* **59,** 1409–1458 (1996).
22. Lee, C. H. *et al.* Magnetic anisotropy in epitaxial Co superlattices. *Phys. Rev. B* **42,** 1066–1069 (1990).
23. Myers, E. B. *et al.* Thermally activated magnetic reversal induced by a spin-polarized current. *Phys. Rev. Lett.* **89,** 196801 (2002).
24. Nazarov, A. V., Cho, H. S., Nowak, J., Stokes, S. & Tabat, N. Tunable ferromagnetic resonance peak in tunneling magnetoresistive sensor structures. *Appl. Phys. Lett.* **81,** 4559–4561 (2002).
25. Sun, J. Z. Spin-current interaction with a monodomain magnetic body: A model study. *Phys. Rev. B* **62,** 570–578 (2000).
26. Bazaliy, Y. B., Jones, B. A. & Zhang, S. C. Towards metallic magnetic memory: How to interpret experimental results on magnetic switching induced by spin-polarized currents. *J. Appl. Phys.* **89,** 6793–6795 (2001).
27. Grollier, J. *et al.* Field dependence of magnetization reversal by spin transfer. *Phys. Rev. B* **67,** 174402 (2003).
28. Li, Z. & Zhang, S. Magnetization dynamics with a spin-transfer torque. *Phys. Rev. B* **68,** 024404 (2003).
29. Suhl, H. The theory of ferromagnetic resonance at high signal powers. *J. Phys. Chem. Solids* **1,** 209–227 (1957).
30. Polianski, M. & Brouwer, P. W. Current-induced transverse spin wave instability in a thin nanomagnet. Preprint at ⟨http://arXiv:cond-mat/0304069⟩ (2003).

Acknowledgements We thank K. W. Lehnert, I. Siddiqi and other members of the groups of R. J. Schoelkopf, D. E. Prober and M. H. Devoret for advice about microwave measurements. We acknowledge support from DARPA through Motorola, from the Army Research Office, and from the NSF/NSEC programme through the Cornell Center for Nanoscale Systems. We also acknowledge use of the NSF-supported Cornell Nanofabrication Facility/NNUN.

Competing interests statement The authors declare that they have no competing financial interests.

Correspondence and requests for materials should be addressed to D.C.R. (ralph@ccmr.cornell.edu).

Video-speed electronic paper based on electrowetting

Robert A. Hayes & B. J. Feenstra

Philips Research Eindhoven, Prof. Holstlaan 4, 5656 AA Eindhoven, The Netherlands

In recent years, a number of different technologies have been proposed for use in reflective displays[1–3]. One of the most appealing applications of a reflective display is electronic paper, which combines the desirable viewing characteristics of conventional printed paper with the ability to manipulate the displayed information electronically. Electronic paper based on the electrophoretic motion of particles inside small capsules has been demonstrated[1] and commercialized; but the response speed of such a system is rather slow, limited by the velocity of the particles. Recently, we have demonstrated that electrowetting is an attractive technology for the rapid manipulation of liquids on a micrometre scale[4]. Here we show that electrowetting can also be used to form the basis of a reflective display that is significantly faster than electrophoretic displays, so that video content can be displayed. Our display principle utilizes the voltage-controlled movement of a coloured oil film adjacent to a white substrate. The reflectivity and contrast of our system approach those of paper. In addition, we demonstrate a colour concept, which is intrinsically four times brighter than reflective liquid-crystal displays[5] and twice as bright as other emerging technologies[1–3]. The principle of microfluidic motion at low voltages is applicable in a wide range of electro-optic devices.

Microfluidic movement based on electrowetting[4,6,7]—where a voltage difference between a hydrophobic solid and a liquid causes a change in wettability—is being used for an increasing number of applications. These include pixelated optical filters[4], adaptive lenses[8] and lab-on-a-chip[9]. Electrowetting has several very attractive features for use in micrometre- to millimetre-sized systems: low power consumption, fast response speed and scalability. In addition, when a fluoropolymer coating with low contact-angle hysteresis is used, a high degree of reversibility can be obtained[4]. However, in most of the applications reported a thick insulator is used, giving rise to high switching voltages. By improving the processing of hydrophobic insulating materials we managed to lower the drive voltages dramatically[10,11], opening up a much broader application area.

For the electrowetting display principle, the focus is on the movement of a confined water–oil interface (Fig. 1). In equilibrium, a coloured oil film lies naturally between the water and the hydrophobic insulator coating of an electrode, because

$$\gamma_{o,w} + \gamma_{o,i} < \gamma_{w,i} \quad (1)$$

where γ is the interfacial tension, and the subscripts denote the oil, water and insulator, respectively. Owing to the dominance of interfacial over gravitational forces in small systems (<2 mm), such an oil film is continuous and stable in all orientations. However, when a voltage V is applied between the substrate electrode and the water, an electrostatic term ($\sim 0.5CV^2$, where C is the parallel-plate capacitance) is added to the energy balance, and the stacked state is no longer energetically favourable (Fig. 1b). The system can lower its energy by moving the water into contact with the insulator, thereby displacing the oil.

The balance between electrical and capillary forces determines how far the oil is moved to the side. Hence the optical properties of the stack, when viewed from above, can be continuously and reversibly tuned between a coloured off-state and a transparent on-state, assuming that the pixel is sufficiently small that a viewer

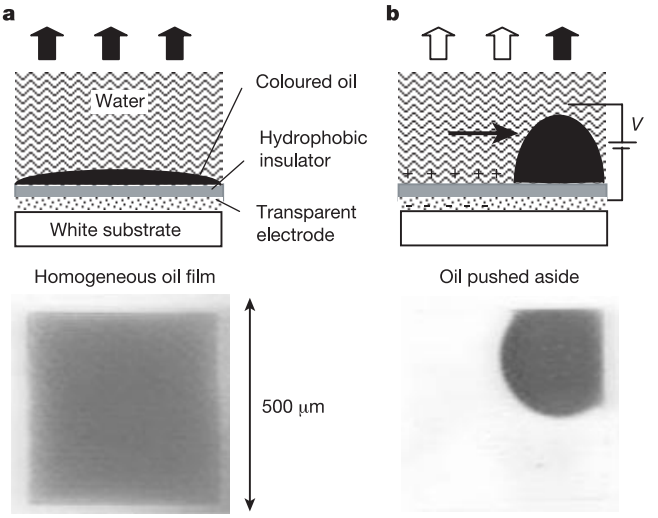

Figure 1 Electrowetting display principle. **a**, No voltage applied, therefore a coloured homogeneous oil film is present. **b**, d.c. voltage applied, causing the oil film to contract. Top row, diagrams; bottom row, photographs. The photographs show typical oil motion obtained with an homogeneous pixel electrode.